Results in Physics 13 (2019) 102166

Contents lists available at ScienceDirect

Results in Physics

journal homepage: www.elsevier.com/locate/rinp

# Investigation of the effects of $Tm^{3+}$ on the structural, microstructural, optical, and magnetic properties of Sr hexaferrites

M.A. Almessiere[a,c,*], Y. Slimani[b], H. Gungunes[d], A. Manikandan[e], A. Baykal[a]

[a] Department of Nano-Medicine Research, Department of Biophysics, Institute for Research & Medical Consultations (IRMC), Imam Abdulrahman Bin Faisal University, P. O. Box 1982, 31441 Dammam, Saudi Arabia
[b] Department of Biophysics, Institute for Research & Medical Consultations (IRMC), Imam Abdulrahman Bin Faisal University, P.O. Box 1982, 31441 Dammam, Saudi Arabia
[c] Department of Physics, College of Science, Imam Abdulrahman Bin Faisal University, P.O. Box 1982, 31441 Dammam, Saudi Arabia
[d] Department of Physics, Hitit University, Çevre Yolu Bulvarı-Çorum 19030, Turkey
[e] Department of Chemistry, Bharath Institute of Higher Education and Research, Bharath University, Chennai 600 073, Tamil Nadu, India

ARTICLE INFO

*Keywords:*
Hexaferrites
Tm substitution
Mossbauer study
Magnetic properties
Optical study
Cation distribution

ABSTRACT

$SrTm_xFe_{12-x}O_4$ ($0.00 \le x \le 0.10$) hexaferrites (HFs) are produced successfully using a sol–gel approach. The structural, optical, and magnetic properties are investigated. The hexagonal phase is confirmed for all the products. The magnetization is measured with respect to the applied magnetic field, M(H). The magnetic parameters including saturation magnetization $M_s$, remanence $M_r$, squareness ratio (SQR = $M_r/M_s$), coercivity $H_c$, and magnetic moment $n_B$ are deduced at room (300 K; RT) and low (10 K) temperatures. It is shown that the ferrimagnetic nature and $Tm^{3+}$ substitutions lead to decreases in the magnetization and coercivity magnitudes. The results on magnetic properties are investigated extensively with respect to the structural and microstructural properties. The SQR values indicate the formation of a single magnetic domain for the x = 0.0 sample and a multi-magnetic domain structure for the $Tm^{3+}$-substituted Sr HFs ($x \ge 0.02$). The obtained $H_c$ values suggest that the produced HFs are promising candidates for potential magnetic recording applications.

## Introduction

Ferrites can be considered as excellent magnetic and dielectric materials for electromagnetic wave absorbers. In comparison to spinel ferrites, hexaferrites (HFs) (for example, $BaFe_{12}O_{19}$ and $SrFe_{12}O_{19}$) with hexagonal magneto-plumbite structure are promising absorbing materials because of their great magneto-crystalline anisotropy, high $M_s$ and $H_c$, excellent chemical stability, and high-frequency application [1,2].

To date, several routes were used for M-type HF synthesis, such as co-precipitation, sol–gel, hydrothermal, and high-energy ball milling [3–6]. The sol–gel auto-combustion approach has the following advantages: simplicity, low cost, highest crystallinity and purity, good chemical homogeneity, low processing time, and fine distribution of particles size, etc. [7,8].

The studies on rare earth (RE) element-substituted M-type HF have increasing significantly over the past several years. The substitution of RE elements into M-type HFs improves both their magneto-crystalline anisotropy and electromagnetic properties [9]. RE ions have strong coupling of 4f–3d angular momentum, which enhances the electromagnetic properties. The 4f shell is practically unaffected by the potential field of neighboring ions, which lead to enhanced coupling [10–12]. The substitutions with ions of lanthanide series like Sm, Gd, Er, Ce, Eu, Nd, Dy, etc in M-type hexaferrites have been studied and revealed an improvement of magnetic and microwave absorption properties [13–19]. I. Ali et al. [20] investigated the structural and magnetic properties of $Tb^{3+}$ substituted M-type hexaferrites prepared through sol–gel auto-combustion method. They found an improvement of $H_c$ values from 1825 to 4440 Oe with $Tb^{3+}$ substitutions, which is mostly attributed to greater magneto-crystalline anisotropy. In addition, it is confirmed that the obtsined $H_c$ and $M_r$ values make the prepared $Tb^{3+}$ substituted M-type hexaferrites useful for high frequency and magnetic recording media applications. M. Jamalian [21] investigated microwave, magnetic and structural properties of Tb-Sn co-substituted Sr HFs synthesized by sol–gel technique. The magnetic findings indicated that $M_s$ and $M_r$ are increased and the coercivity $H_c$ is decreased with increasing Sn-Tb substitutions.

The preparation of single-phase RE-substituted HFs is still a challenge and the properties of such products are required to be explored

* Corresponding author. Tel.: +00966505807292.
*E-mail address:* malmessiere@iau.edu.sa (M.A. Almessiere).

https://doi.org/10.1016/j.rinp.2019.102166
Received 5 February 2019; Received in revised form 28 February 2019; Accepted 1 March 2019
Available online 07 March 2019

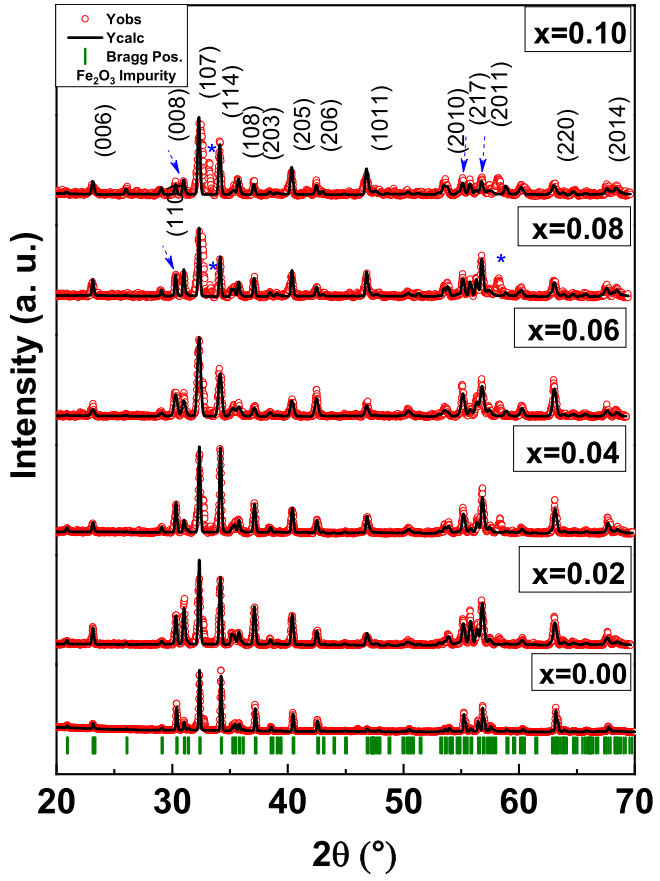


**Fig. 1.** XRD powder patterns of $SrTm_xFe_{12-x}O_{19}$ ($0.00 \leq x \leq 0.10$) hexaferrites.

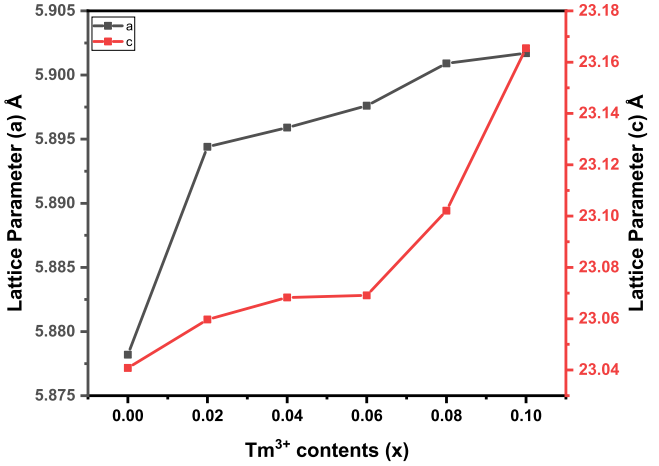


**Fig. 2.** Evolution of lattice parameters 'a' and 'c' versus $Tm^{3+}$ contents.

systematically. To the best of our knowledge, there is no study investigating up to date the influence of $Tm^{3+}$ substitutions on the properties of Sr M-type hexaferrites. Accordingly, we report in this study and for the first time the impact of $Tm^{3+}$ substitutions on structural, morphological, spectral, optical and magnetic properties of Sr HFs. Various samples of $SrTm_xFe_{12-x}O_4$ (x = 0.00, 0.02, 0.04, 0.06, 0.08, 0.10) have been produced via a citrate sol-gel auto-combustion approach.

## Experimental

### *Chemicals and instrumentation*

$Sr(NO_3)_2{\cdot}4H_2O$ (99%) and $FeCl_3{\cdot}9H_2O$ (98%) were received from Sigma Aldrich, and $Tm_2O_3$ (99%) was obtained from US Research Nanomaterials, Inc. They were used without further purification. The structural information was examined through X-ray diffraction (XRD; Rigaku Miniflex) and Fourier transform infrared spectrometry (FTIR; Bruker alpha II). Scanning and transmission electron microscopy (SEM, TEM; FEI S/TEM Titan 300) with energy-dispersive X-ray spectroscopy (EDX) and elemental mapping were used for morphological and microstructural observations. The optical measurements were performed through UV–vis diffuse reflectance (%DR) spectrophotometry. Mössbauer spectra were recorded using a standard Mössbauer spectrometer (Fast Com Tec PC-moss II) under constant acceleration mode using $^{57}Fe$ in Rh matrix with an approximate activity of 10 m Ci. The spectra were examined with the help of Win-Normos fitting software. Hysteresis loops were performer by using vibrating sample magnetometry (VSM).

### *Synthesis*

For the typical synthesis, a stock solution of Sr and Fe chemicals in de-ionized water (DI) was prepared in a 100 ml beaker using stoichiometric amounts of the respective metal salts and stirred for 15 min. A stoichiometric amount of $Tm_2O_3$ was also dissolved in 10 ml conc. HCl + 10 ml DI water under vigorous stirring. Then, these two solutions were mixed in a 200 ml beaker and heated at 80 °C under constant stirring. Citric acid was added to the metal solution (molar ratio 1:1.5). To adjust the pH to 7.0, ammonia solution was added. The solution was gradually evaporated at 80 °C until a viscous gel is obtained. The temperature was increased to approximately 250 °C to ignite the gel. The resulting powders were heated at 1100 °C for 5 h.

**Table 1**
Tm content, refined structural parameters for $SrTm_xFe_{12-x}O_{19}$ ($0.00 \leq x \leq 0.10$) HFs with space group $P6_3/mmc$.

| x | $a = b$ (Å) | $C$ (Å) | $V$ (Å)$^3$ | $c/a$ | $D_{XRD}$ (nm) ± 0.05 | $\chi^2(chi^2)$ | $R_{Bragg}$ | $Rwp$ | $Rexp$ |
|---|---|---|---|---|---|---|---|---|---|
| 0.00 | 5.878(2) | 23.040(8) | 689.46 | 3.9197 | 46.83 | 1.61 | 18.14 | 36.8 | 30.3 |
| 0.02 | 5.894(4) | 23.059(7) | 693.85 | 3.9121 | 42.89 | 2.16 | 10.89 | 43.8 | 27.9 |
| 0.04 | 5.895(9) | 23.068(3) | 694.47 | 3.9126 | 43.96 | 2.20 | 12.79 | 38.9 | 26.1 |
| 0.06 | 5.897(6) | 23.069(1) | 694.89 | 3.9116 | 27.50 | 1.98 | 9.06 | 41.5 | 25.4 |
| 0.08 | 5.900(9) | 23.102(1) | 697.84 | 3.9150 | 35.63 | 1.99 | 23.72 | 41.0 | 25.1 |
| 0.10 | 5.901(7) | 23.165(4) | 696.36 | 3.925 | 41.75 | 2.84 | 24.69 | 36.8 | 30.3 |

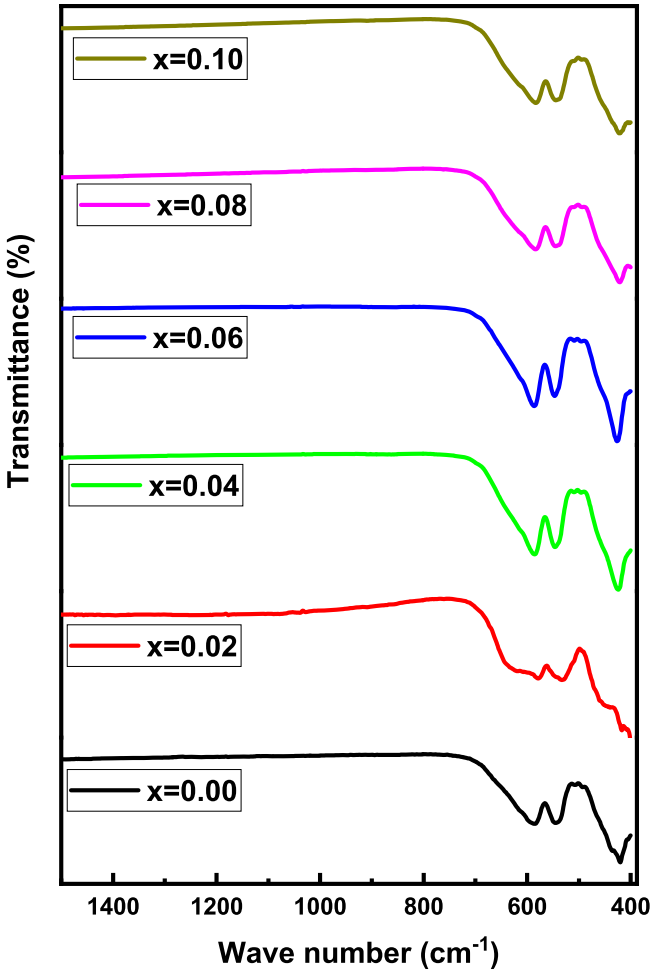


**Fig. 3.** FT-IR spectra of $SrTm_xFe_{12-x}O_{19}$ ($0.00 \le x \le 0.10$) hexaferrites.

**Table 2**
FTIR vibration bands and force constant at tetrahedral and octahedral positions of $SrTm_xFe_{12-x}O_{19}$ ($0.00 \le x \le 0.10$) HFs.

| Tm content (x) | $(\nu 1)cm^{-1}$ | $(\nu 2)cm^{-1}$ | $F_{CT}\times 10^5$ (dynes/cm$^2$) | $F_{CO}\times 10^5$ (dynes/cm$^2$) |
|---|---|---|---|---|
| 0.00 | 587.84 | 422.92 | 2.52 | 1.30 |
| 0.02 | 594.16 | 413.13 | 2.58 | 1.25 |
| 0.04 | 585.74 | 424.46 | 2.51 | 1.35 |
| 0.06 | 587.38 | 428.21 | 2.52 | 1.34 |
| 0.08 | 585.90 | 421.82 | 2.51 | 1.30 |
| 0.10 | 584.44 | 422.13 | 2.50 | 1.31 |

## Results and discussion

### *XRD examinations*

XRD patterns of $SrTm_xFe_{12-x}O_4$ ($0.00 \le x \le 0.10$) HFs are presented in Fig. 1. Different peaks are indexed according to the JCPDS Card 00-043-0002 of Sr HF. Minor peaks related to $Fe_2O_3$ were found at high concentrations of 0.08 and 0.10. The XRD results indicate that the lattice parameters "a" and "c" increase. c increases faster (0.54%) than a (0.39%), which means that the c-axis undergoes more expansion than the a-axis owing to Tm substitution, and hence the volume of the cell also increases as listied in (Table 1) [2,14,22]. This may be due to the ionic radius difference between $r_{Tm3+}$ (1.02 Å) and $r_{Fe3+}$ (0.67 Å) (Fig. 2). The c/a ratio ranges between 3.91 and 3.92, which confirms that the M-type hexagonal structure is formed [23,24].

### *FT-IR investigation*

FT-IR spectra of $SrTm_xFe_{12-x}O_4$ ($0.00 \le x \le 0.10$) HFs are given in Fig. 3. The spectra illustrate stretching vibration bands at 422.92 and 587.84 $cm^{-1}$ corresponding to metal–oxygen stretching vibrations corresponding to octahedral and tetrahedral sites [16,25]. The FT-IR spectrum of sintered samples have identical absorption bands that confirmed the formation of hexagonal structure with on-existence of any absorption band to un reactant elements. Additionally, It is clear that the vibration band at 587.84 $cm^{-1}$ is shifted toward the higher at $x = 0.02$ then to lower wave numbers for the rest of ratios, whereas the 422.92 $cm^{-1}$ shifted toward higher wave number except $x = 0.08$ and 0.10. These results are due to change the length of Fe-O bands in tetrahedral (A-site) and octahedral (B-site) caused by the Tm substituting [26,27]. Force constant of the characteristic vibration bands of FT-IR spectra have been calculated and listed in Table 2 [28].

### *Microstructural analysis*

SEM micrographs of Tm-substituted $SrTm_xFe_{12-x}O_{19}$ ($x = 0.00$, 0.02, and 0.08) HFs are depicted in Fig. 4. These images reveal that the grains have a hexagonal plate shape with a high rate of aggregation. Clearly, the grain sizes are larger than crystallites, owing to the assemblage of small grains forming larger particles. EDX and elemental mapping results of $SrFe_{12-x}Tm_xO_{19}$ ($x = 0.02$ and 0.08) are presented in Fig. 5. These show that the element weight is matched with the prepared compositions, without any external elements. The $x = 0.04$ sample was characterized by TEM and high-resolution TEM (HRTEM), which showed aggregates of single crystals. The HRTEM images exhibited a hexagonal symmetry consistent the hexagonal $SrFe_{12}O_{19}$ crystal phases 114 and 307, as displayed in Fig. 6.

### *Optical measurements*

A DR-UV-visible spectrophotometer was employed to explore the optical characteristics of $SrTm_xFe_{12-x}O_4$ ($0.00 \le x \le 0.10$) HFs. The obtained spectra are presented in Fig. 7. All the products absorbed light in the visible range. The band gap energy ($E_g$) was estimated through the Kubelka–Munk model [29]. A Tauc plot, $(\alpha h\nu)^2$ vs. $(h\nu)$, was used to calculate the $E_g$ values for $SrTm_xFe_{12-x}O_4$ ($0.00 \le x \le 0.10$) HFs (Fig. 8). As shown, the band gap values for the $x = 0.00$, 0.02, 0.04, 0.06, 0.08, and 0.10 HFs are 1.75, 1.93, 1.77, 2.00, 2.18, and 2.08 eV, respectively. It is obvious that when the $Tm^{3+}$ content increases, the $E_g$ value also increases. The increased band gap energy may be due to the development of interface defects or energy levels [30].

### *Mossbauer analysis*

Mössbauer spectra of $SrTm_xFe_{12-x}O_4$ ($0.00 \le x \le 0.10$) HFs are presented in Fig. 9. The deduced parameters are given in Table 3. The fitted Mössbauer spectra presented five sextets, which are related to five different crystallographic sites, as shown in Table 2. These sextets are correlated to the existence of $Fe^{3+}$ ion in the octahedral (12 k, $4f_2$, and 2a), tetrahedral ($4f_1$), and trigonal (2b) sites of the hexagonal structure [31,32]. This structure consists of three spins-up (2a, 2b, and 12 k) and two spins-down ($4f_1$, $4f_2$) sublattices for $Fe^{3+}$ ions [33]. In addition, one superparamagnetic doublet was formed apart from the ferromagnetic sextets for the doped samples. The existence of the doublet in the

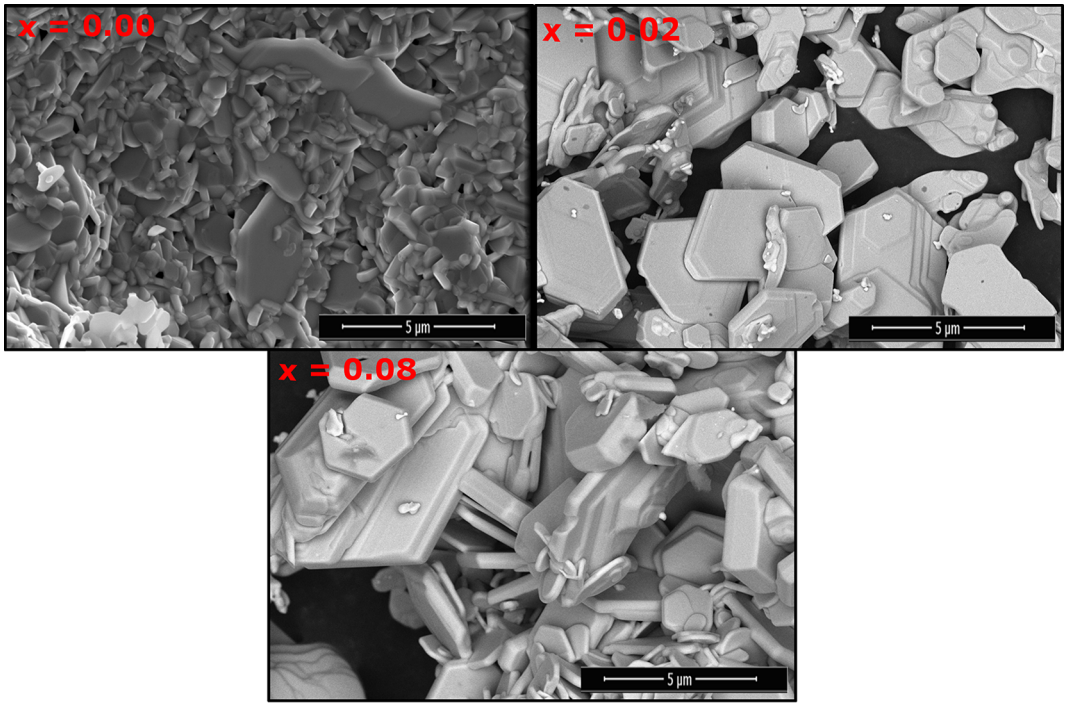


**Fig. 4.** SEM micrographs of $SrTm_xFe_{12-x}O_{19}$ (x = 0.00, 0.02 and 0.08) hexaferrites.

Mössbauer spectrum shows that some particles with paramagnetic characteristics are present in the matrix. The relative area ($R_A$) of the doublet increased with increasing doped ion concentration. The isomer shift (IS) takes values between 0.262 and 0.391 mm/s. For magnetically ordered phases, the IS of $Fe^{3+}$ changes between 0.05 and 0.5 mm $s^{-1}$ [34]. Consequently, the obtained IS corresponds to the characteristic $Fe^{3+}$ charge state. The IS of the $4f_1$ site increases, whereas that of the 2a site decreases with increasing doped ion concentration, which indicates that the s electron density of the $Fe^{3+}$ ions at the $4f_1$ and 2a sites is affected by the $Tm^{3+}$ substitution. With increasing x, the quadrupole splitting (QS) of the $4f_2$ and 2b sites is marginally increased, although that of the $4f_1$ site is slightly decreased. The hyperfine field $B_{hf}$ for the five Fe sublattices was determined to be ordered as follows: $B_{hf}$ (2b) < $B_{hf}$ (12 k) < $B_{hf}$ ($4f_1$) < $B_{hf}$ (2a) < $B_{hf}$ ($4f_2$). The $B_{hf}$ of all the sites decrease slightly with increasing $Tm^{3+}$ content. The observed decrease could be ascribed to the nonmagnetic $Tm^{3+}$ ions replacing the $Fe^{3+}$ ions. This replacement leads to a decrement in the super-exchange interaction among the ions.

The distribution of the $R_A$ of all the sextet sites, which is directly proportional to the number of $Fe^{3+}$ ions, is given in Fig. 10. The $R_A$ of the doublet increases and those of the 12 k and 2b sites continuously decreased with increasing doped ions. The $R_A$ of the 2a site increased as x increased to 0.04, and then decreased. Generally, it is known that doped ions with larger size go to octahedral sites, but smaller ones occupy tetrahedral sites [35]. Accordingly, one can affirm that $Tm^{3+}$ (1.03 Å) ions occupy the 12 k site up to x = 0.04 then occupy 12 k and 2a sites.

*Magnetization measurement*

The measurements of the magnetization with respect to the applied magnetic field, M(H), were performed for all $SrTm_xFe_{12-x}O_4$ ($0.00 \leq x \leq 0.10$) HFs using VSM with H = ± 10 kOe. The M(H) curves and various deduced magnetic parameters for the all HFs acquired at RT are illustrated in Fig. 11 and Table 4, respectively. It is shown that the Tm substitution at Fe sites strongly affected the magnetic properties. The remanent magnetization ($M_r$) is ranged from 6.88 to 41.78 emu/g. $H_c$ was in the range of 224.5–433.7 Oe. The $M_{max}$ (magnetization at maximum field of 10 kOe) values were found to be between 51.8 and 64.5 emu/g. Clearly, 10 kOe was insufficient to saturate the produced HFs. For that reason, the Stoner–Wohlfarth (S–W) approximation is used to extract the saturation magnetization ($M_s$) [36-38]. Fig. 11(b) shows the plots of M vs. $1/H^2$ for all the $SrTm_xFe_{12-x}O_4$ ($0.00 \leq x \leq 0.10$) HFs at RT. The extrapolation of these plots at high magnetic fields (above 5 kOe) in approaching 0 yields the $M_s$ values. It is found that the $M_s$ values vary between 50.08 and 70.07 emu/g at RT. According to the obtained results, the different produced $SrTm_xFe_{12-x}O_4$ HFs present a hard ferrimagnetic (FM) nature at RT.

The M(H) were also measured for all $SrTm_xFe_{12-x}O_4$ ($0.00 \leq x \leq 0.10$) HFs at 10 K, as presented in Fig. 12. The deduced magnetic parameters at 10 K are tabulated in Table 3. $H_c$ varies between 2015 and 3366 Oe. $M_r$ is in the range 36.6–45.9 emu/g. The $M_{max}$ values are in a range of 78.6–88.2 emu/g. The externally applied field of ± 10 kOe is almost insufficient to reach saturation magnetization magnitudes for all samples at 10 K. Indeed, the $M_s$ magnitudes were determined using the S–W approximation as at RT and, and the estimated values are listed in Table 3. $M_s$ varies from 80.8 to 96.7 emu/g. The obtained results at 10 K reveal the FM nature of all the HFs. Compared to 300 K, the magnetization magnitudes show a noticeable increase at 10 K. This increment is principally due to the reduced thermal fluctuations of the magnetic moments [39,40]. However, for the same x content level and with decreasing temperature from RT to

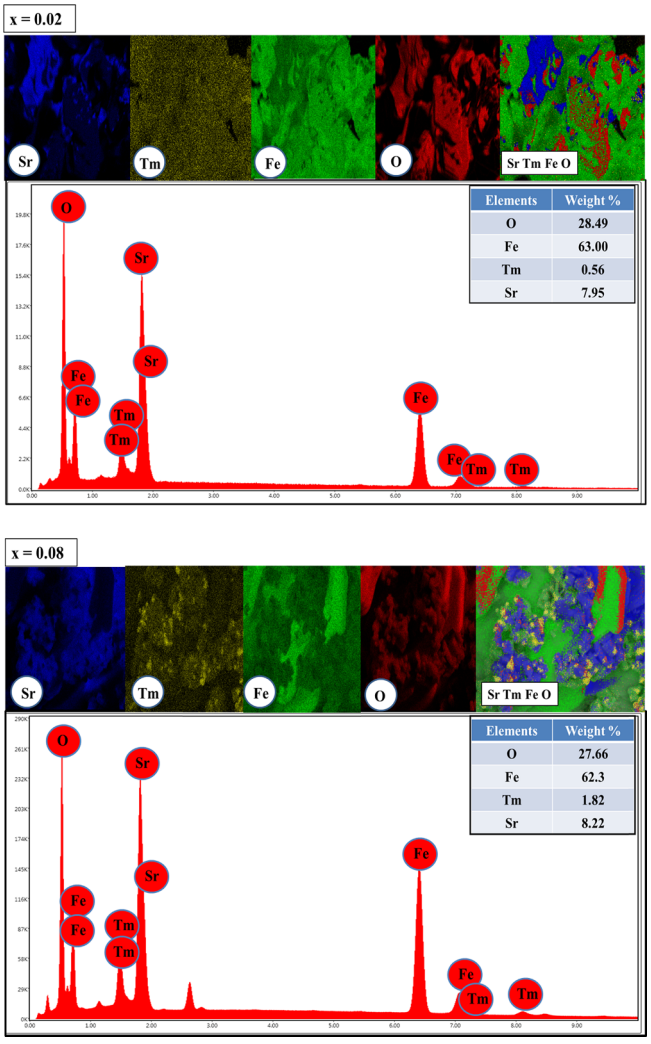


**Fig. 5.** Elemental mapping results for $SrTm_xFe_{12-x}O_{19}$ (x = 0.02 and 0.08) hexaferrites.

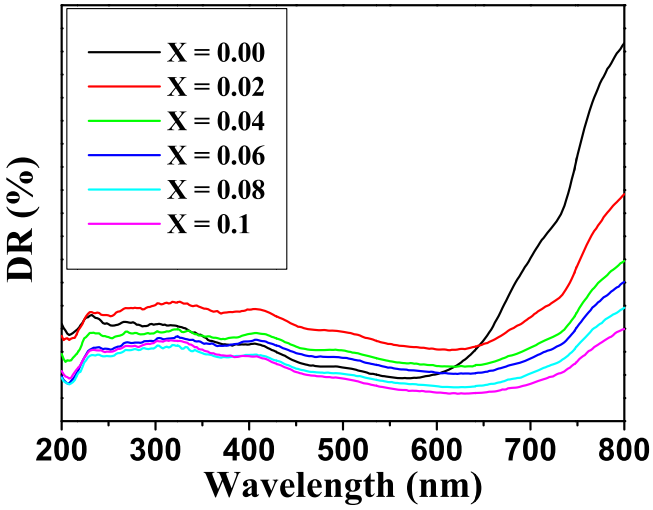


**Fig. 7.** %DR spectra of $SrTm_xFe_{12-x}O_{19}$ ($0.00 \leq x \leq 0.10$) hexaferrites.

10 K, the coercivity $H_c$ reduces. This reduction with the decrease of temperature is mainly correlated with the change in the $M_s$ values. Actually, when $M_s$ improves with decreasing the temperature from RT to lower temperature, $H_c$ diminishes too [41,42]. In the present investigation, it is found that the $M_s$ values increase with decreasing the temperature from RT to 10 K. Therefore, the reduction in $H_c$ values is attributed to the increase in $M_s$ when decreasing the temperature from RT to 10 K.

Fig. 13 shows the evolutions of the $M_s$, $M_r$, and $H_c$ values as a function of the $Tm^{3+}$ content at both RT and 10 K. The non-substituted sample $SrFe_{12}O_{19}$ (x = 0.0) shows $M_s$ magnitudes equal to 70.07 and 97.86 emu/g at 300 and 10 K, respectively. The $M_s$ magnitudes found in this study are larger than those reported in Sr-Cr HFs produced through a microwave hydrothermal method [43], Sr HFs synthesized via a hydrothermal method [44], K-Ta-substituted Sr HFs [45], and $SrTi_2Co_2Fe_8O_{19}$ single crystal [46]. As the $Tm^{3+}$ substitution content increases, the $M_s$ magnitude decreased remarkably at both RT and 10 K. The minimum $M_s$ values were observed for the $SrFe_{11.9}Tm_{0.1}O_{19}$ (x = 0.1) product, with magnitudes of approximately 50.08 and 76.95 emu/g at 300 and 10 K, respectively. Similar trends have been discerned in various RE-substituted Sr HFs (RE = Sm, Nd, La, Gd, Er, Ce, Y) [47–49]. It is known that numerous factors can affect the magnetic properties of HFs including the variations of crystallites size/grains size, variations in the magnetic moments ($n_B$), strains, super-exchange interactions between different ions, variations in the nature and concentration of different sites, and the preferred site occupancy of different ions [19,39,40].

Generally, the magnetic moment of HFs is derived from the iron ions and their distribution in the crystal sites. Indeed, the $Fe^{3+}$-O-

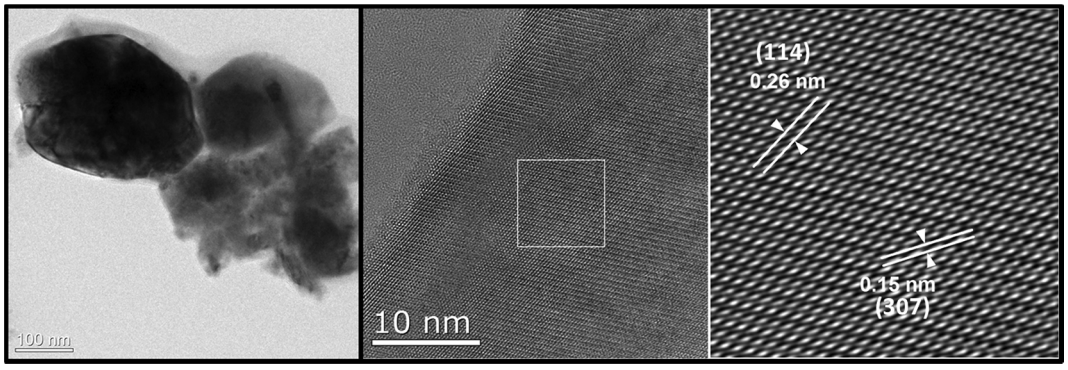


**Fig. 6.** TEM images of $SrTm_{0.04}Fe_{11.96}O_{19}$ hexaferrite.

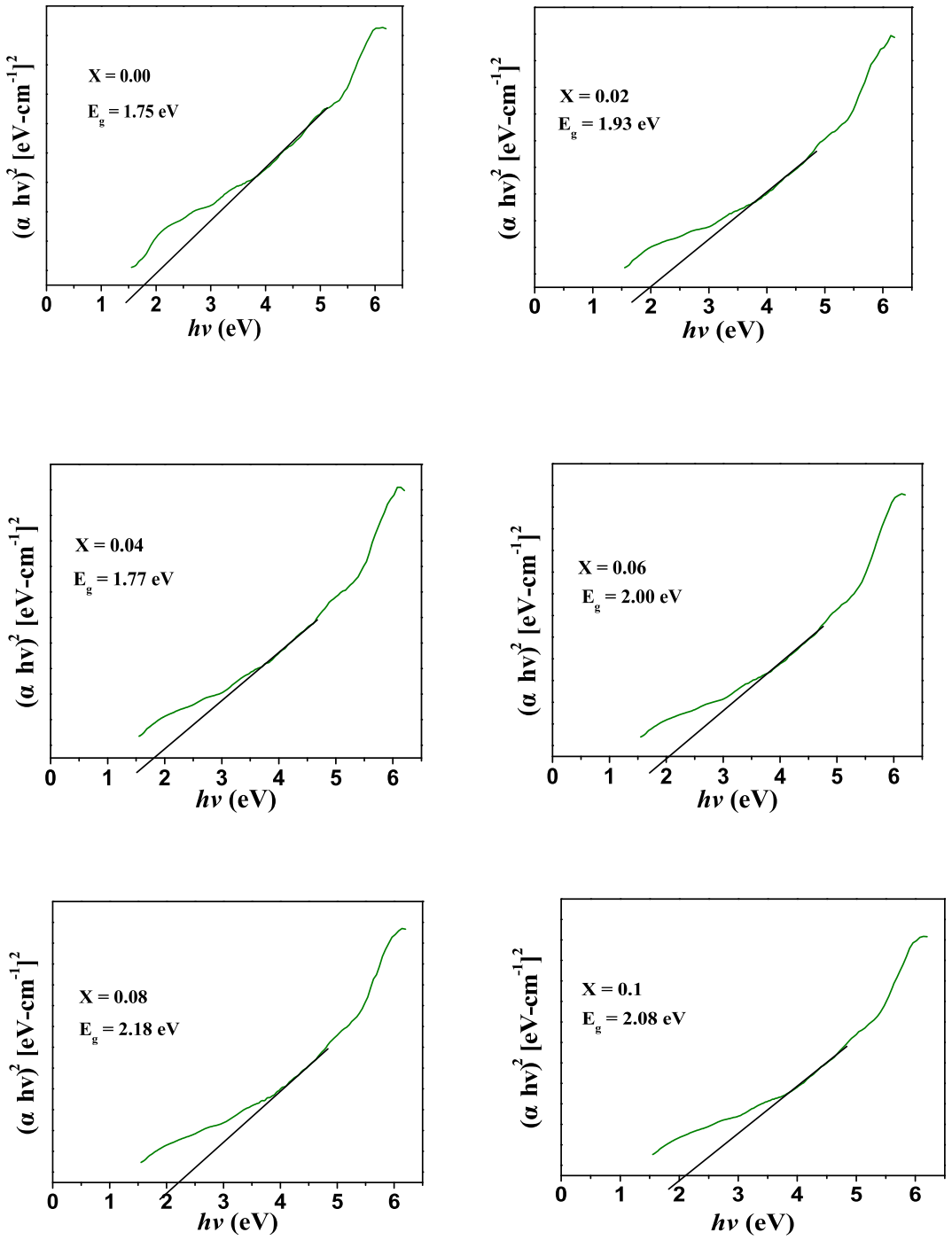


**Fig. 8.** Tauc plots of $SrTm_xFe_{12-x}O_{19}$ ($0.00 \leq x \leq 0.10$) hexaferrites.

$Fe^{3+}$ exchange interactions are the dominant compared to the other $Sr^{2+}$-O-$Sr^{2+}$ and $Sr^{2+}$-O-$Fe^{3+}$ interactions. Therefore, any factors that affect the strength of the $Fe^{3+}$-O-$Fe^{3+}$ exchange interaction will modify the magnetization. In addition, it is known that in the RE-substituted HFs products, $Fe^{3+}$-O-$RE^{3+}$ interactions will occur via the 4f–3d couplings [50]. These interactions are very weak because they are resulted from the indirect 4f–5d–4f coupling [50]. In the present study, the observed decrease in the $M_s$ values at both RT and 10 K with increasing $Tm^{3+}$ content is attributed to the weakening of the super-exchange interactions in the Fe sites. Moreover, the magnetic moments in Sr HFs resulted from iron ions that reside in the five different sublattices: the 12 k, $4f_2$, 2a, 2b, and $4f_1$ sites. It is reported that if the substitution occurred in the spins-down, the magnetization increases [40]. If the substitution occurred in the spins-up, the magnetization decreases [40].

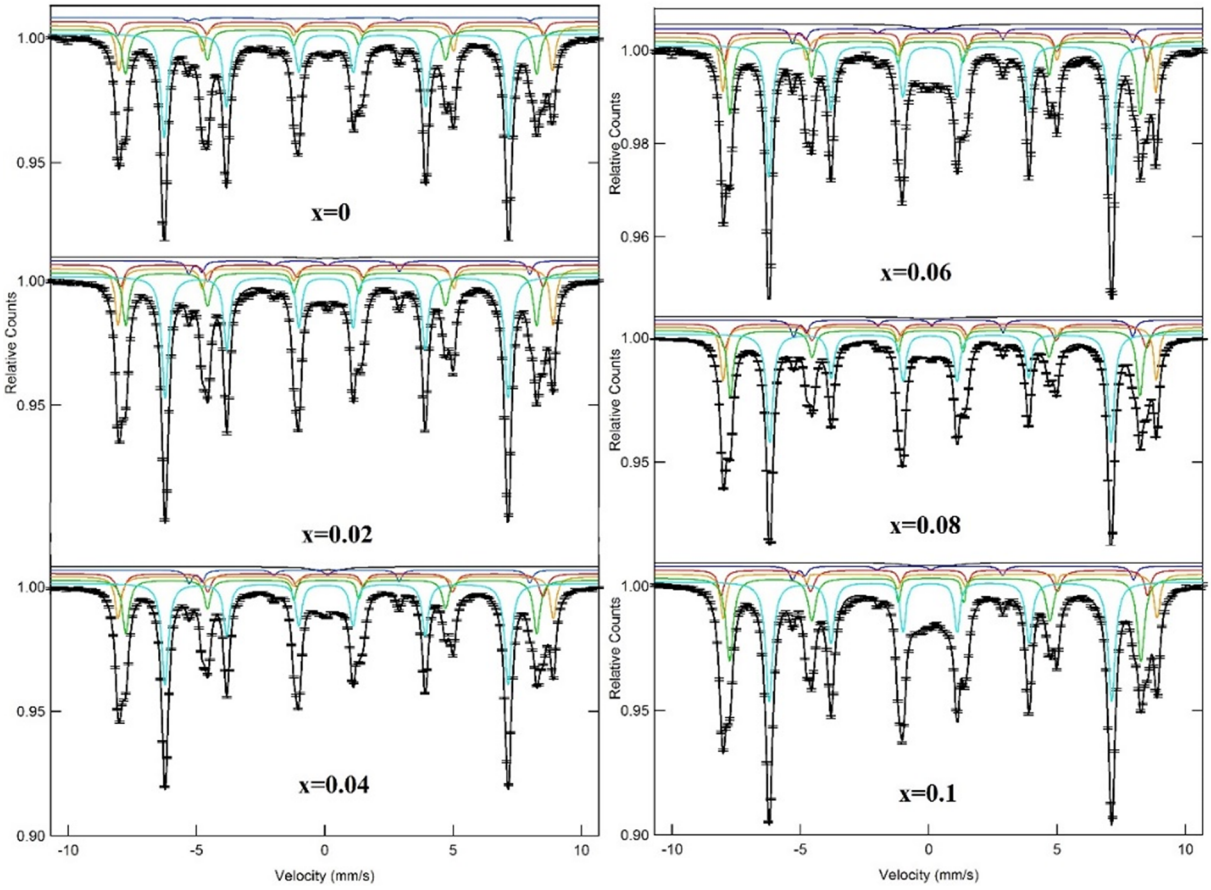


**Fig. 9.** Room Temperature Mössbauer spectra of $SrTm_xFe_{12-x}O_4$ ($0.00 \leq x \leq 0.10$) hexaferrites.

Accordingly, it can be confirmed that the $Tm^{3+}$ ions prefer to occupy the spins-up iron sites, which is in accordance with Mossbauer results. Furthermore, the substitution of $Fe^{3+}$ ions having magnetic moment of 5 $\mu_B$ (where $\mu_B$ is the Bohr magneton) by $Tm^{3+}$ ions having lower magnetic moment of 1.6 $\mu_B$ could explain the decrease in the $M_s$ values at both RT and 10 K. Additionally, the difference in ionic radii ($r_{Fe^{3+}}$ = 0.64 Å and $r_{Tm^{3+}}$ = 1.09 Å) causes an enlargement of the distance between the magnetic ions. This leads to diminish the strength of the super-exchange interaction. Moreover, the contrast in the ionic radii ($r_{Fe^{3+}}$ = 0.64 Å and $r_{Tm^{3+}}$ = 1.09 Å) and magnetic moments of the substituted and host ions might engender a non-collinear ferromagnetic arrangement and local strains that generate disorder and variations in the electronic states of the HF systems [19,40]. The relation between $n_B$ and $M_s$ is given by [51]:

$$n_B = \frac{Molecular\ Weight\ x\ M_s}{5585}$$

Table 4 reports the estimated $n_B$ values of all prepared HFs at both 300 and 10 K. Generally, the decrease in $n_B$ is resulted from the weakening of the super-exchange interactions among various sites. In the present study, the x = 0.0 product displays the greatest $n_B$ and $M_s$ values at both RT and 10 K. These values decrease at both RT and 10 K with increasing $Tm^{3+}$ substitution content. The obtained findings indicate a weakening of the super-exchange interactions at both RT and 10 K.

It has been reported previously that the evolutions in $M_r$ depend primarily on the evolutions in $M_s$ and on the net alignment of the magnetization grains derived from the super-exchange interactions between magnetic particles [39]. For these reasons, a similar trend can be observed in $M_r$ at both RT and 10 K (Fig. 13.b). $M_r$ is extreme for x = 0.0, with magnitudes of approximately 41.78 and 54.55 emu/g at 300 and 10 K, respectively. $M_r$ decreases sharply at both RT and 10 K with increasing $Tm^{3+}$ content. The squareness ratios (SQR = $M_r/M_s$) were calculated for all the $SrTm_xFe_{12-x}O_4$ ($0.00 \leq x \leq 0.10$) HFs at 300 and 10 K and are listed in Table 3. An SQR below 0.5 indicates that the nanoparticles were in the multi-magnetic domain; however, an SQR greater than or equal to 0.5 reveals the development of a single magnetic domain structure [52]. The SQRs for the non-substituted product were equal to 0.596 and 0.557 at 300 and 10 K, respectively, which indicates that this sample is in the single magnetic domain at both RT and 10 K. However, the SQR values are below 0.5 at both RT and 10 K for $x \geq 0.02$ indicating the formation of multi-domain structures in all the substituted products at both RT and 10 K.

$H_c$ decreases in a remarkable way at both RT and 10 K with increasing the $Tm^{3+}$ substitution content. The highest obtained values for x = 0.0 are approximately 4333.7 and 2819.1 Oe at 300 and 10 K, respectively. The minimum $H_c$ magnitudes are observed for x = 0.1 with values of 224.5 and 204.4 Oe at 300 and 10 K, respectively. Various parameters governed the coercivity, such as the morphology, grains size, shape, magnetic anisotropy, and spin canting [39,40]. Numerous

**Table 3**
Mössbauer Spectra parameters of $SrFe_{12-x}Tm_xO_{19}$ ($0.00 \le x \le 0.10$). $B_{hf}$: Hyperfine Magnetic Field, I.S: Isomer Shift, Q.S: Quadrupole Splitting, W: Line Width, and $R_A$: Relative Area.

| Sample | Site | $B_{hf}$ (T) ( ± 0.004) | I.S (mm/s)( ± 0.003) | Q.S (mm/s) ( ± 0.005) | $R_A$ (%) |
|---|---|---|---|---|---|
| $SrFe_{12}O_{19}$ | 12 k | 41.485 | 0.357 | 0.398 | 48.381 |
| | 4f1 | 49.716 | 0.262 | 0.176 | 17.771 |
| | 4f2 | 52.735 | 0.379 | 0.292 | 13.924 |
| | 2a | 51.185 | 0.323 | 0.016 | 11.679 |
| | 2b | 41.237 | 0.318 | 2.282 | 8.2449 |
| $SrFe_{11.98}Tm_{0.02}O_{19}$ | 12 k | 41.412 | 0.36 | 0.412 | 46.961 |
| | 4f1 | 49.643 | 0.265 | 0.182 | 18.084 |
| | 4f2 | 52.553 | 0.381 | 0.291 | 12.654 |
| | 2a | 51.044 | 0.352 | 0.068 | 12.918 |
| | 2b | 41.194 | 0.309 | 2.284 | 5.4656 |
| | Db | – | 0.212 | 0.908 | 3.9172 |
| $SrFe_{11.96}Tm_{0.04}O_{19}$ | 12 k | 41.446 | 0.36 | 0.413 | 46.823 |
| | 4f1 | 49.655 | 0.264 | 0.188 | 15.377 |
| | 4f2 | 52.568 | 0.38 | 0.302 | 12.571 |
| | 2a | 51.054 | 0.348 | 0.061 | 14.853 |
| | 2b | 41.143 | 0.312 | 2.291 | 5.0953 |
| | Db | – | 0.24 | 0.75 | 5.2806 |
| $SrFe_{11.94}Tm_{0.06}O_{19}$ | 12 k | 41.409 | 0.355 | 0.406 | 45.673 |
| | 4f1 | 49.599 | 0.262 | 0.179 | 17.055 |
| | 4f2 | 52.348 | 0.374 | 0.292 | 15.113 |
| | 2a | 51.087 | 0.355 | 0.029 | 10.729 |
| | 2b | 41.142 | 0.292 | 2.275 | 4.9994 |
| | Db | – | 0.229 | 0.822 | 6.4326 |
| $SrFe_{11.92}Tm_{0.08}O_{19}$ | 12 k | 41.24 | 0.36 | 0.41 | 45.338 |
| | 4f1 | 49.462 | 0.268 | 0.175 | 17.186 |
| | 4f2 | 52.341 | 0.381 | 0.307 | 12.716 |
| | 2a | 50.958 | 0.348 | 0.057 | 11.486 |
| | 2b | 40.983 | 0.310 | 2.279 | 5.5069 |
| | Db | – | 0.22 | 0.734 | 7.7673 |
| $SrFe_{11.90}Tm_{0.10}O_{19}$ | 12 k | 41.375 | 0.361 | 0.409 | 43.375 |
| | 4f1 | 49.674 | 0.277 | 0.166 | 17.707 |
| | 4f2 | 52.378 | 0.391 | 0.319 | 11.898 |
| | 2a | 51.505 | 0.32 | 0.013 | 10.346 |
| | 2b | 41.195 | 0.291 | 2.306 | 4.1082 |
| | Db | – | 0.239 | 1.23 | 12.566 |

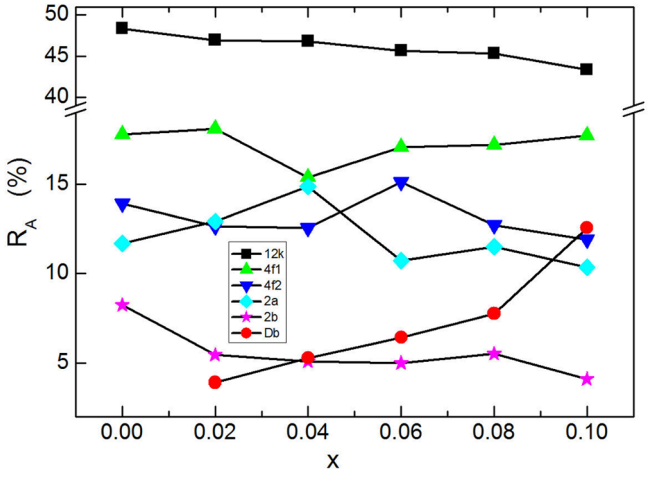


**Fig. 10.** Variation in relative area ($R_A$) of different sites with Tm content.

studies have revealed that products exhibiting low $H_c$ are advantageous for magnetic recording applications such as video tapes, floppy disks, and hard disks [53]. From the current investigation, we note that $H_c$ ranges from 224.5 to 4333.7 Oe at RT and from 204.4 to 2819.1 Oe at 10 K for various $Tm^{3+}$-substituted Sr HFs ($0.0 \le x \le 0.1$), which suggests that the prepared HF products may be beneficial for permanent magnets and high-density recording media.

## Conclusion

$SrTm_xFe_{12-x}O_4$ ($0.00 \le x \le 0.10$) was fabricated through citrate sol–gel process. The Sr HF structure was confirmed by XRD, FT-IR, SEM, and TEM studies. The average crystallite size was determined to range from 27 to 46 nm. The lattice parameters increased with increasing $Tm^{3+}$ content. %DR spectra showed that the optical band gap increased with increasing substitution content. Mössbauer spectra revealed that one superparamagnetic doublet formed in addition to ferromagnetic sextets in the doped samples. The distribution of the $R_A$ showed that the $Tm^{3+}$ (1.03 Å) ions occupy the 12 k site up to $x = 0.04$ and then occupy the 12 k and 2a sites. The analyses of M(H) hysteresis loops showed a ferrimagnetic behavior for various HFs at both 300 and 10 K. The magnetic parameters strongly depend on the temperature and the $Tm^{3+}$ substitution contents. The deduced $M_s$, $M_r$, $H_c$, and $n_B$ values decrease with increasing the $Tm^{3+}$ content at both RT and 10 K. This effect is due to the weakening of the super-exchange interactions, the creation of local strains, the preferred site occupancy, the dissimilarity of ionic radii, and the decrease in the magnetic moments ($n_B$) with substitutions. The calculated SQR values indicated a single magnetic

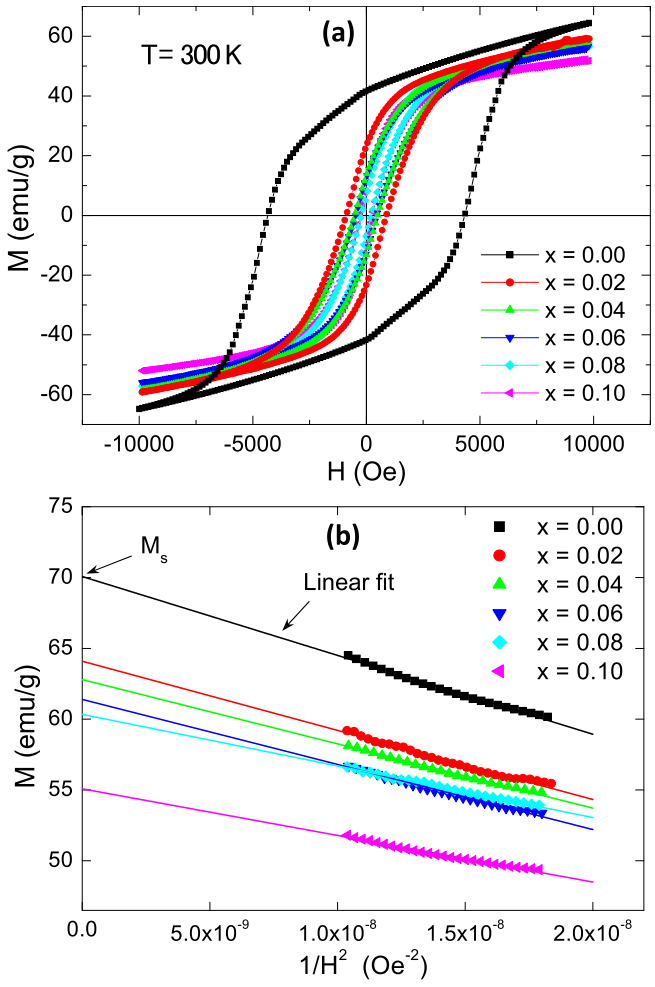


**Fig. 11. (a)** M (H) curves and **(b)** M vs $1/H^2$ plots for all $SrTm_xFe_{12-x}O_4$ (x = 0.00, 0.02, 0.04, 0.06, 0.08, 0.1) hexaferrites performed at RT.

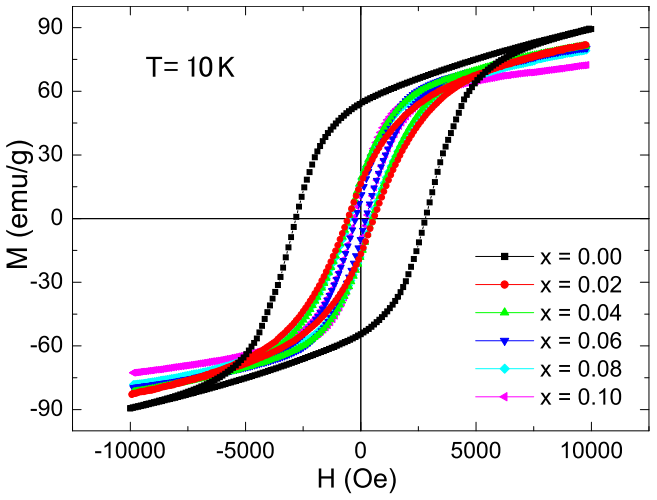


**Fig. 12.** M (H) curves for all $SrTm_xFe_{12-x}O_4$ (x = 0.00, 0.02, 0.04, 0.06, 0.08, 0.1) hexaferrites performed at 10 K.

domain for the non-substituted product and the creation of multi-domain structures in the $Tm^{3+}$-substituted products. The obtained $H_c$ values suggest that the produced HFs could be promising candidates for high-density recording media and permanent magnets.

## Acknowledgments

The Institute for Research & Medical Consultations (Projects application No. 2017-IRMC-S-3, No. 2018-IRMC-S-1 and No. 2018- IRMC-S-2) of Imam Abdulrahman Bin Faisal University (Saudi Arabia) is acknowledged for its financial support.

**Table 4**
Magnetic parameters of all $SrFe_{12-x}Tm_xO_{19}$ $SrTm_xFe_{12-x}O_4$ (x = 0.00, 0.02, 0.04, 0.06, 0.08, 0.1) hexaferrites at RT and 10 K.

| *T = 300* K | | | | | | |
|---|---|---|---|---|---|---|
| x | $M_{max}$ (emu/g) | $M_s$ (emu/g) | $M_r$ (emu/g) | *SQR* | $H_c$ (Oe) | $n_B(\mu_B)$ |
| 0.00 | 64.5 | 70.07 | 41.78 | 0.596 | 4333.7 | 13.32 |
| 0.02 | 59.2 | 64.08 | 23.41 | 0.365 | 897.7 | 12.21 |
| 0.04 | 58.1 | 62.79 | 13.41 | 0.214 | 511.5 | 11.99 |
| 0.06 | 56.7 | 61.40 | 12.80 | 0.208 | 504.0 | 11.75 |
| 0.08 | 56.5 | 60.34 | 9.58 | 0.159 | 271.3 | 11.57 |
| 0.10 | 51.8 | 50.08 | 6.88 | 0.137 | 224.5 | 9.62 |
| *T = 10* K | | | | | | |
| x | $M_{max}$ (emu/g) | $M_s$ (emu/g) | $M_r$ (emu/g) | *SQR* | $H_c$ (Oe) | $n_B(\mu_B)$ |
| 0.00 | 89.5 | 97.86 | 54.55 | 0.557 | 2819.1 | 18.60 |
| 0.02 | 81.8 | 89.94 | 25.11 | 0.306 | 578.4 | 17.13 |
| 0.04 | 81.2 | 87.73 | 17.99 | 0.205 | 474.4 | 16.75 |
| 0.06 | 80.3 | 86.72 | 16.52 | 0.190 | 471.5 | 16.59 |
| 0.08 | 79.2 | 85.79 | 13.40 | 0.156 | 250.3 | 16.45 |
| 0.10 | 72.4 | 76.95 | 9.61 | 0.125 | 204.4 | 14.78 |

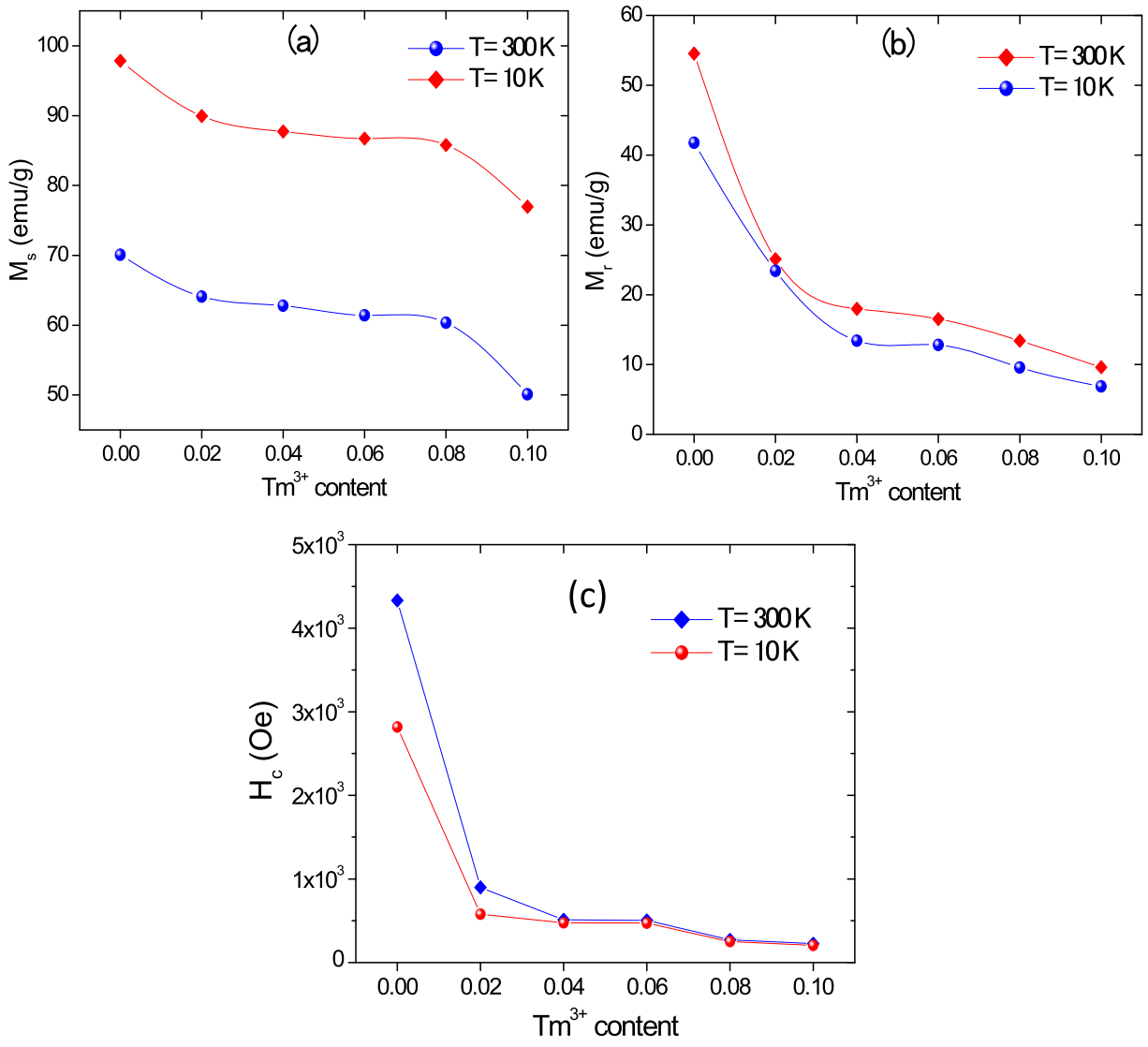


**Fig. 13.** Variations of **(a)** $M_s$, **(b)** $M_r$ and **(c)** $H_c$ versus $Tm^{3+}$ content for various $SrTm_xFe_{12-x}O_4$ (x = 0.00, 0.02, 0.04, 0.06, 0.08, 0.1) hexaferrites at 300 and 10 K.

## References


[1] Chawla SK, Mudsainiyan RK, Meen SS, Yusuf SM. Sol–gel synthesis, structural and magnetic properties of nanoscale M-type barium hexaferrites $BaCo_xZr_xFe_{(12-2x)}O_{19}$. J Magn Magn Mater 2014;350:23–9.

[2] Deng L, Zhao Y, Xie Z, Liu Z, Tao C, Deng R. Magnetic and microwave absorbing properties of low-temperature sintered $BaZr_xFe_{12}$-$xO_{19}$. RSC Adv 2018;8:42009–16.

[3] Ben Ghzaiel T, Dhaoui W, Pasko A, Mazaleyrat F. Effect of non-magnetic and magnetic trivalent ion substitutions on BaM-ferrite properties synthesized by hydrothermal method. J Alloy Compd 2016;671:245–53.

[4] Pashkova EV, Solovyova ED, Kolodiazhnyi TV, Ivanitskii VP, Belous AG. Effect of heat treatment on the phase composition, structure and magnetic properties of M-type barium hexaferrite. J Magn Magn Mater 2014;368:1–7.

[5] Alsmadi AM, Bsoul I, Mahmood SH, Alnawashi G, Prokes K, Siemensmeyer K, et al. Magnetic study of M-type doped barium hexaferrite nanocrystalline particles. J Appl Phys 2013;114:243910.

[6] Baykal A, Auwal IA, Guner S, Sozeri H. Magnetic and optical properties of $Zn^{2+}$ ion substituted barium hexaferrites. J Magn Magn Mater 2017;430:29–35.

[7] Sutka A, Mezinskis G. Sol–gel auto-combustion synthesis of spinel-type ferrite nanomaterials. Front Mater Sci 2012;6(2):128–41.

[8] Du Y, Liu Y, Lian L, Du J. Structural and magnetic properties of $Sr_{0.8}La_{0.2}Co_{0.2}Fe_{11.8-x}Al_xO_{19}$ hexaferrite particles prepared via sol-gel auto-combustion method. J Magn Magn Mater 2019;469:189–95.

[9] Luo J, Xu Y, Mao H. Magnetic and microwave absorption properties of rare earth ions ($Sm^{3+}$, $Er^{3+}$) doped strontium ferrite and its nano composites with polypyrrole. J Magn Magn Mater 2015;381:365–71.

[10] Sadiq I, Naseem S, Ashiq MN, Iqbal MA, Ali I, Khan MA, et al. Spin canting effect and microwave absorption properties of Sm-Mn substituted nanosized material. J Magn Magn Mater 2015;395:159–65.

[11] Wang L, Zhang J, Zhang Q, Xu N, Song J. XAFS and XPS studies on site occupation of $Sm^{3+}$ ions in Sm doped M-type $BaFe_{12}O_{19}$. J Magn Magn Mater 2015;377:362–7.

[12] Auwal IA, Baykal A, Güngünes H, Shirsath SE. Structural investigation and hyperfine interactions of $BaBi_xLa_xFe_{12-2x}O_{19}$($0.0 \leq x \leq 0.5$) hexaferrites. Ceram Int 2016;42:338–3387.

[13] Rehmana KMU, Riaz M, Liu X, Khan MW, Yang Y, Batood KM, et al. Magnetic properties of Ce doped M-type strontium hexaferrites synthesized by ceramic route. J Magn Magn Mater 2019;474:83–9.

[14] Almessiere MA, Slimani Y, Baykal A. Structural and magnetic properties of Ce-doped strontium hexaferrite. Ceram Int 2018;44:9000–8.

[15] Rezlescu N, Doroftei C, Rezlescu E, Popa PD. The influence of heat-treatment on microstructure and magnetic properties of rare-earth substituted $SrFe_{12}O_{19}$. J Alloy Compd 2008;451:492–6.

[16] Auwal IA, Baykal A, Güner S, Sertkol M, Sözeri H. Magneto-optical properties $BaBi_xLa_xFe_{12-2x}O_{19}$ ($0.0 \leq x \leq 0.5$) hexaferrites. J Magn Magn Mater 2016;409:92–8.

[17] Auwal IA, Güner S, Güngüneş H, Baykal A. $Sr_{1-x}La_xFe_{12}O_{19}$ ($0.0 \leq x \leq 0.5$) hexaferrites: synthesis, characterizations, hyperfine interactions and magneto-optical properties. Ceram Int 2016;42:12995–3003.

[18] Güner S, Auwal IA, Baykal A, Sözeri H. Synthesis, characterization and magneto optical properties of $BaBi_xLa_xY_xFe_{12-3x}O_{19}$ ($0.0 \leq x \leq 0.33$) hexaferrites. J Magn Magn Mater 2016;416:261–8.

[19] Almessiere MA, Slimani Y, Baykal A. Impact of Nd-Zn co-substitution on microstructure and magnetic properties of $SrFe_{12}O_{19}$ nanohexaferrite. Ceram Int 2019;45:963–9.

[20] Ihsan Ali MU, Islam MS Awan, Ahmad Mukhtar, Muhammad, Ashiq Naeem, Naseem Shahzad. Effect of $Tb^{3+}$ substitution on the structural and magnetic properties of M-type hexaferrites synthesized by sol–gel auto-combustion technique. J Alloy Compd 2013;550:564–72.

[21] Jamalian M. An investigation of structural, magnetic and microwave properties of strontium hexaferrite nanoparticles prepared by a sol–gel process with doping SN and Tb. J Magn Magn Mater 2015;378:217–20.

[22] Almessiere MA, Slimani Y, Tashkandi NA, Baykal A, Saraç MF, Trukhanov AV, et al. The effect of Nb substitution on magnetic properties of $BaFe_{12}O_{19}$ nanohexaferrites.

Ceram Int 2019;45:1691–7.
[23] Topkaya R, Auwal I, Baykal A. Effect of temperature on magnetic properties of $BaY_xFe_{12-x}O_{19}$ hexaferrites. Ceram Int 2016;42:16296–302.
[24] Wagner TR. Preparation and crystal structure analysis of magneto-plumbite-type $BaGa_{12}O_{19}$. J Solid State Chem 1998;136:120.
[25] Auwal IA, Güngüneş H, Baykal A, Güner S, Shirsath Sagar E, Sertkol M, et al. Structural, morphological, optical, cation distribution and Mössbauer analysis of $Bi^{3+}$ substituted strontium hexaferrite. Ceram Int 2016;42:8627–35.
[26] Kumar R, Kar M. Correlation between lattice strain and magnetic behavior in non-magnetic Ca substituted nano-crystalline cobalt ferrite. Ceram Int 2016;42(6):6640–7.
[27] Ahmad SI, Ansari SA, Kumar DR. Structural, morphological, magnetic properties and cation distribution of Ce and Sm co-substituted nano crystalline cobalt ferrite. Mater Chem Phys 2018;208:248–57.
[28] Cullity BD, Graham CD. Introduction to Magnetic Materials. 2nd ed. Wiley-IEEE Press; 2008. ISBN 978-0-471-47741-9.
[29] Slimani Y, Güngüneş H, Nawaz M, Manikandan A, El Sayed HS, Almessiere MA, Sözeri H, Shirsath SE, Ercan I, Baykal A. Magneto-optical and microstructural properties of spinel cubic copper ferrites with Li-Al co substitution. Ceram Int 2018;44(2018):14242–50.
[30] Li X, Hou Y, Zhao Q, Wang L. A general, one-step and template-free synthesis of sphere-like zinc ferrite nanostructures with enhanced photocatalytic activity for dye degradation. J Colloids Interface Sci 2011;358:102.
[31] Awawdeh M, Bsoul I, Mahmood SH. Magnetic properties and Mössbauer spectroscopy on Ga, Al, and Cr substituted hexaferrites. J Alloy Compd 2014;585:465–73.
[32] Galvao SB, Lima AC, de Medeiros SN, Soares JM, Paskocimas CA. The effect of the morphology on the magnetic properties of barium hexaferrite synthesized by Pechini method. Mater Lett 2014;115:38–41.
[33] Solovyova ED, Pashkova EV, Ivanitski VP, Vyunov OI, Belous AG. Mössbauer and X-ray diffraction study of $Co^{2+}$–$Si^{4+}$ substituted M-type barium hexaferrite $BaFe_{12-2x}Co_xSi_xO_{19\pm\gamma}$. J Magn Magn Mater 2013;330:72–5.
[34] Hodges P, Short S, Jorgensen JD, Xiong X, Dabrovski B, Mini SM, et al. Evolution of oxygen-vacancy ordered crystal structures in the perovskite series $SrnFe_nO_{3n-1}$ (n= 2, 4, 8, and∞), and the relationship to electronic and magnetic. J Solid State Chem 2000;151:190–209.
[35] Lalegani Z, Nemati A. Effects of Ce–Co substitution on structural, magnetic and dielectric properties of M-type barium hexaferrite nanoparticles synthetized by sol–gel auto. J Mater Sci: Mater Electron 2015;26:2134–44.
[36] Stoner EC, Wohlfarth EP. A mechanism of magnetic hysteresis in heteregeneous alloys. Philos Trans R Soc A 1948;240(826):599–642.
[37] Almessiere MA, Slimani Y, Baykal A. Exchange spring magnetic behavior of $Sr_{0.3}Ba_{0.4}Pb_{0.3}Fe_{12}O_{19}/(CuFe_2O_4)_x$ nanocomposites fabricated by a one-pot citrate sol-gel combustion method. J Alloy Compd 2018;762:389–97.
[38] Almessiere MA, Demir Korkmaz A, Slimani Y, Nawaz M, Ali S, Baykal A. Magneto-optical properties of rare earth metals substituted Co-Zn spinel nanoferrites. Ceram Int 2019;45:3449–58.
[39] Almessiere MA, Slimani Y, Baykal A. Structural and magnetic properties of Ce doped strontium hexaferrite. Ceram Int 2018;44:9000.
[40] Almessiere MA, Slimani Y, El Sayed HS, Baykal A, Ercan I. Microstructural and magnetic investigation of vanadium-substituted Sr-nanohexaferrite. J Magn Magn Mater 2019;471:124–32.
[41] Almessiere MA, Slimani Y, El Sayed HS, Baykal A, Ali S, Ercan I. Investigation of microstructural and magnetic properties of $BaV_xFe_{12-x}O_{19}$ nanohexaferrites. J Supercond Nov Magn 2018. https://doi.org/10.1007/s10948-018-4856-8.
[42] Slimani Y, Almessiere MA, Nawaz M, Baykal A, Akhtar S, Ercan I, et al. Effect of bimetallic (Ca, Mg) substitution on magneto-optical properties of $NiFe_2O_4$ nanoparticles. Ceram Int 2018. https://doi.org/10.1016/j.ceramint.2018.12.072.
[43] Katlakunta S, Meena SS, Srinath S, Bououdina M, Sandhya R, Praveena K. Improved magnetic properties of $Cr^{3+}$ doped $SrFe_{12}O_{19}$ synthesized via microwave hydrothermal route. Mater Res Bull 2015;63:58–66.
[44] Xia A, Zuo C, Chen L, Jin C, Lv Y. Hexagonal $SrFe_{12}O_{19}$ ferrites: hydrothermal synthesis and their sintering properties. J Magn Magn Mater 2013;332:186–91.
[45] Ashiq MN, Qureshi RB, Malana MA, Ehsan MF. Fabrication, structural, dielectric and magnetic properties of tantalum and potassium doped M-type strontium calcium hexaferrites. J Alloy Compd 2015;651:266–72.
[46] Mihalik M, Sirenko V, Balbashov AM, Eremenko V, Mihalik M, Zentková M. The magnetic properties of single crystal $SrCo_2Ti_2Fe_8O_{19}$ compound. Phys Proc 2015;75:259–65.
[47] Rezlescu N, Doroftei C, Rezlescu E, Popa PD. The influence of heat-treatment on microstructure and magnetic properties of rare earth substituted $SrFe_{12}O_{19}$. J Alloy Compd 2008;451:492–6.
[48] Singh A, Bindra Narang S, Kulwant Singh OP, Pandey RK Kotnala. Electrical and magnetic properties of rare earth substituted strontium hexaferrites. J Ceram Proc Res 2010;11:241–9.
[49] Almessiere MA, Slimani Y, El Sayed HS, Baykal A. Structural and magnetic properties of Ce-Y substituted strontium nanohexaferrites. Ceram Int 2018;44:12511–9.
[50] Iqbal MJ, Farooq S. Impact of Pr–Ni substitution on the electrical and magnetic properties of chemically derived nanosized strontium–barium hexaferrites. J Alloy Compd 2010;505:560–7.
[51] Almessiere MA, Slimani Y, Baykal A. Structural, morphological and magnetic properties of hard/soft $SrFe_{12-x}V_xO_{19}/(Ni_{0.5}Mn_{0.5}Fe_2O_4)_y$ nanocomposites: effect of vanadium substitution. J Alloy Compd 2018;767:966–75.
[52] Ali I, Islam MU, Awan MS, Ahmad M, Ashiq MN, Naseem S. Effect of $Tb^{3+}$ substitution on the structural and magnetic properties of M-type hexaferrites synthesized by sol–gel auto-combustion technique. J Alloy Compd 2013;550:564–72.
[53] Fu Y-P, Lin C-H. Fe/Sr ratio effect on magnetic properties of strontium ferrite powders synthesized by microwave-induced combustion process. J Alloy Compd 2005;386:222–7.